Published in final edited form as:
Nat Med. 2008 August ; 14(8): 882–888. doi:10.1038/nm.1727.

Adenovirus-mediated gene expression imaging to directly detect sentinel lymph node metastasis of prostate cancer

Jeremy B Burton[1], **Mai Johnson**[2], **Makoto Sato**[2], **Sok Boon S Koh**[3], **David J Mulholland**[1], **David Stout**[1], **Arion F Chatziioannou**[1], **Michael E Phelps**[1], **Hong Wu**[1], and **Lily Wu**[1,2,3]

[1] Department of Molecular and Medical Pharmacology, Crump Institute for Molecular Imaging and Jonsson Comprehensive Cancer Center, David Geffen School of Medicine, University of California–Los Angeles, Los Angeles, California 90095-1735, USA

[2] Department of Urology, Crump Institute for Molecular Imaging and Jonsson Comprehensive Cancer Center, David Geffen School of Medicine, University of California–Los Angeles, Los Angeles, California 90095-1735, USA

[3] Department of Bioengineering, Crump Institute for Molecular Imaging and Jonsson Comprehensive Cancer Center, David Geffen School of Medicine, University of California–Los Angeles, Los Angeles, California 90095-1735, USA

Abstract

The accurate assessment of nodal involvement in prostate cancer is crucial to planning treatment, yet there is a shortage of noninvasive imaging techniques capable of visualizing nodal lesions directly. This study demonstrates the feasibility of using recombinant human adenoviral vectors to detect nodal metastases in a human prostate cancer model. This was achieved by the prostate-restricted expression of optical and positron emission tomography (PET) imaging reporter genes by the viral vector coupled with the innate lymphotropic properties of adenovirus. We show that peritumoral administration of these vectors results in the direct detection of reporter gene expression in metastatic lesions within sentinel lymph nodes. Notably, this approach parallels the current lymphoscintigraphy method but enables the direct PET visualization of sentinel lymph node metastases, eliminating the need for invasive lymphadenectomy. These findings may lead to more effective diagnostic and therapeutic strategies for individuals with advanced-stage prostate cancer.

The pathological findings of aggressive prostate cancer have been well documented in a large series of prostatectomy subjects[1,2]. Among the adverse pathologic features, the presence of pelvic lymph node metastasis is the strongest predictor of poor outcome[3]. For instance, the 10-year progression-free survival probabilities were 79% for organ-confined disease, 53% for disease with extraprostatic extension and only 12% for disease with lymph node metastases[1].

Correspondence should be addressed to L.W. lwu@mednet.ucla.edu.

Note: Supplementary information is available on the Nature Medicine website.

COMPETING INTERESTS STATEMENT

The authors declare competing financial interests: details accompany the full-text HTML version of the paper at http://www.nature.com/naturemedicine/.

AUTHOR CONTRIBUTIONS

J.B.B. performed most of the experiments and prepared the manuscript. M.J. assisted in mouse imaging. M.S. prepared the adenoviral vectors. S.B.S.K. prepared the fluorescent-tagged virus. D.J.M. and H.W. provided the *Pten*-null mice and helpful advice. D.S., A.F.C. and M.E.P. provided imaging technical support. L.W. supervised the project.

Therefore, methods to accurately detect nodal metastasis would be very helpful for tumor staging and in formulating the most appropriate treatment.

Despite the importance of nodal status of prostate cancer, methods to assess pelvic lymph nodes are suboptimal. At the present time, accurate lymph node staging can only be determined by pelvic lymphadenectomy[4]. Potential complications of this procedure include lymphoceles, lymphedema, venous thrombosis and pulmonary embolism, with an estimated incidence of 20%[5]. Conventional imaging modalities such as computed tomography (CT) and magnetic resonance imaging (MRI) are useful in evaluating anatomical abnormalities; however, neither technology can differentiate between adenopathy related to inflammation and that caused by deposition of malignant cells[6,7]. Recently, a new iron oxide paramagnetic nano-particle was developed as an MRI contrast agent to identify tumor-infiltrated lymph nodes in individuals with prostate cancer[8]. However, this technology relies on an indirect identification of metastasis in which nodal infiltration of macrophages that have engulfed the magnetic particles highlight metastatic regions devoid of signal.

Advancements in sentinel lymph node (SLN) mapping have come mainly from the melanoma and breast cancer fields[9,10]. The current method of intraoperative lymphoscintigraphy entails the use of a γ camera to monitor the transit of a technetium-99m (^{99m}Tc)-filtered sulfur colloid particle from the peritumoral injection site into the SLN, which is then harvested for histopathological examination[11]. The size and surface properties of colloidal particles determine their suitability as lymphangiographic agents[11,12]. Studies have implicated the ability of human adenovirus (serotype 5) to be effectively transported into the lymphatic circulation[13–15]. The negatively charged capsid and size (~100 nm) probably favor the entry of adenoviral particles into the lymphatics.

We have developed several prostate-specific adenoviral vectors that express imaging reporter genes under the control of a highly amplified prostate-specific antigen (PSA) promoter system, known as the two-step transcriptional activation (TSTA) system[16,17]. Here we demonstrate that adenoviral vectors effectively function as lymphotropic agents and can mediate gene transfer into the metastatic prostate cancer cells in the draining lymph nodes. Such a prostate-specific gene expression imaging modality may be very helpful toward improving the clinical management of advanced stage prostate cancer.

RESULTS

Adenovirus traffics via lymphatics to regional lymph nodes

As described extensively in the rat, injection of colloidal dyes into the lymphatic-rich front footpad results in their accumulation in the ipsilateral brachial and axillary nodes[18]. To verify that adenoviruses also traverse through the lymphatics, we injected fluorescently tagged AdTSTA-fl, an adenoviral vector expressing firefly luciferase, in the forepaw. After 24 h, we detected the particles in the brachial lymph nodes by immunofluorescence microscopy (Fig. 1a). The number of viral genomes transported to and retained in the brachial node after 24 h averaged about 60,000 copies, yielding an estimated efficiency of delivery of less than 0.1% (Fig. 1b). We next investigated whether the virus was transported to the lymph nodes as free infectious virus. After paw-directed injection of adenoviral vector, the draining lymph nodes were isolated and gently disrupted. The lymph node supernatants were applied to LNCaP prostate cancer cells to evaluate transduction efficiency. In concordance with the PCR distribution data (Fig. 1b), transduction activity (luciferase bioluminescence) was present in the ipsilateral brachial and axillary lymph node but not in the contralateral nodes (Fig. 1c).

To explore the feasibility of the adenoviral lymphangiographic approach in cancerous prostate glands, we examined whether virus could effectively drain to regional lymph nodes in the

mouse prostate *Pten* tumor suppressor gene knockout model[19]. This *Pten*$^{-/-}$ model effectively recapitulates the clinical characteristics of prostate cancer progression, from preneoplastic lesions to frank carcinoma and metastatic disease[19]. The carcinomatous prostate glands from 10-week-old Pten$^{-/-}$ mice are enlarged compared to those from wild-type littermates (Fig. 1d). At this age, *Pten*$^{-/-}$ mice show large lymphatics within stromal regions between cancerous ductules (Fig. 1e). One hour after injecting AdTSTA-fl into each dorsolateral lobe, we observed accumulation of virus within regional lymph nodes (Fig. 1f,**g**). Approximately 1% of the injected dose was recovered in the periaortic lumbar nodes, with a lesser amount in more distant mesenteric and renal lymph nodes. Collectively, these data suggest that adenovirus can function as a lymphotropic agent while retaining gene transfer activity within the targeted lymph nodes.

We surmised that macrophages would not be an effective cellular vehicle for the adenoviral vectors, as the infectivity of mouse macrophage cell lines is more than 10,000 times lower than in a prostate carcinoma cell line (Supplementary Fig. 1a online). Further, extensive *in vivo* applications have shown the selective expression of TSTA imaging reporter vectors in prostate cells positive for androgen receptor (AR) and PSA and not in cells of other tissue origin, such as macrophages and hepatocytes[16,17,20,21] (Supplementary Fig. 1b,c). Moreover, TSTA vector–mediated transgene expression was observed only in tumor cells and not in the associated F4/80^{+} macrophages (Supplementary Fig. 1b).

Lymph node metastasis model of prostate cancer

Our recent findings have shown that the lymphangiogenic vascular endothelial growth factor-C (VEGF-C) promotes lymphatic metastasis in our prostate cancer models[22]. The androgen-dependent, AR^{+}PSA^{+} LAPC-9 (Los Angeles prostate cancer series 9) xenograft model is useful for this diagnostic imaging study because, upon induced expression of VEGF-C, this tumor (LAPC-9–VEGF-C–GFP) shows consistent lymphatic metastasis when implanted subcutaneously (Fig. 2)[22,23]. The tumor cells, transduced with a lentivirus encoding *Renilla* luciferase (RL) as a reporter gene (LAPC-9–VEGF-C–GFP–RL), enabled bioluminescence imaging of tumor growth (Fig. 2a) and sensitive quantification of nodal metastases (Fig. 2b,**c**). Moreover, the volume of nodal infiltration could be adjusted with resection of the primary tumor (Fig. 2a,**d**,**e**). Without primary tumor resection, micrometastases in the brachial or axillary node were consistently observed when the tumors reached about 1 cm in diameter at 3–4 weeks after implantation (Fig. 2a,**b**). However, if the primary tumors were surgically resected and disseminated lesions were allowed to grow for an additional 30–40 d, then large macroscopic metastatic lesions developed, ultimately infiltrating the entire lymph node (Fig. 2d,**e**). This large expansion of the nodal metastases can be monitored in resected mice by repetitive radionuclide PET with ^{18}F-3′-fluoro-3′-deoxy-L-thymidine (^{18}FLT; Fig. 2d). For example, the dissemination of the highly aggressive prostate carcinoma model CWR22Rv-1–VEGF-C can be observed by repetitive ^{18}FLT PET (Supplementary Video 1 online). However, our experience indicated that metabolic PET imaging with ^{18}FLT or ^{18}FDG is insensitive for the LAPC-9 and CWR22Rv-1 human prostate tumor model and requires palpable macroscopic infiltration for reliable detection.

Detecting macrometastasis in draining lymph nodes

Despite the above noted inefficient degree of vector delivery to the axillary lymph nodes by paw-directed injection, we selected this method to show the principle of our approach for the following reasons. First, the paw-directed administrations consistently drained to brachial and axillary nodes (Fig. 1), which were the precise dissemination sites of the subcutaneous prostate tumors implanted in the upper back. Second, the forepaw is at a sufficient distance from the target tissue to ensure a lymphatic route of vector distribution and to rule out random diffusion to the regional target. Third, injection at the forepaw allows for accurate differentiation between luminescent signal emitted from the injection site and that emitted from the targeted lymph

node. To visualize the nodal metastasis by noninvasive imaging, we employed an adenoviral vector capable of expressing an imaging reporter gene at a robust level and in a prostate-specific manner[16] (Fig. 3a). The specificity of AdTSTA–fl was retained in the paw-directed injection as compared to a constitutive CMV promoter driven vector (Supplementary Fig. 1c). The observed paw signals could be attributed to the great magnitude of extravasated vector that remained at the injection site. We tested the diagnostic capabilities of prostate-specific imaging vectors by bioluminescence imaging (Fig. 3b) and PET (Fig. 3c) in mice expected to bear macroscopic nodal lesions. After paw-directed administration of AdTSTA–fl, we detected a clear optical signal in the axillas of tumor-bearing mice but not in controls (Fig. 3b). Considering that specific and precise three-dimensional localization of nodal metastasis will be of great clinical use, we assessed the utility of a prostate-specific TSTA PET reporter vector (AdTSTA–sr39tk)[17] in conjunction with its tracer 9-(4-[^{18}F]fluoro-3-hydroxymethylbutyl) guanine (^{18}FHBG). Injecting AdTSTA–sr39tk into both forepaws produced a positive signal in the ipsilateral but not contralateral axilla (Fig. 3c). The presence of disseminated prostate tumor cells in the ipsilateral brachial lymph node was confirmed by the node's enlarged size, by its GFP fluorescent signal and by histological identification of extensive tumor cell infiltration (Fig. 3d,**e**). The maximum diameter of the infiltrated node was 2.54 mm, two- to threefold larger than the nonmetastatic contralateral node. Tumor cell–localized expression of sr39tk was verified in the respective lymph nodes by immunohistological staining (Fig. 3e).

Direct detection of occult lymph node metastases

Having shown the ability to detect macroscopic nodal lesions, we proceeded to determine the ability of our gene expression vector to detect microscopic metastases. A cohort of 12 mice bearing LAPC-9–VEGF-C–GFP–RL tumors of 1 cm diameter on the right upper back was divided into two subgroups that received either 1×10^8 or 1×10^7 PFU of AdTSTA–fl in both paws (Fig. 4a,**b**). A specific signal was generated only in the ipsilateral axilla of mice that received the higher dose of vector (Fig. 4a,**b**). This finding suggests that the lower dose of virus was insufficient to produce a visible optical signal for the occult metastasis.

We next investigated delivering the AdTSTA–sr39tk in a manner emulating the clinical method of lymphoscintigraphy[11]. After injection around the subcutaneous LAPC-9–VEGF-C–GFP–RL tumor, the viral particles would be expected to drain to the SLN and transduce the metastatic prostate tumor cells. Indeed, robust ^{18}FHBG PET signals were detected in the tumor and the draining axillary lymph node (Fig. 4c). The PET signal of the tumor and the anterior axillary node can be clearly distinguished by sagittal and transverse tomographic views (Fig. 4c) and a three-dimensional rendered digital movie (Supplementary Video 2 online). Immediately after the PET-CT scan, ipsilateral and contralateral lymph nodes were removed, and their bioluminescence and radioactivity were measured (Fig. 4d). Comparison of *ex vivo* radioactive signals showed at least twice the counts per minute per gram tissue in the ipsilateral over the contralateral nodes (Fig. 4d). Moreover, the elevated radioactive tracer activity also correlated with the presence of tumor cells, as verified by the *Renilla* luciferase activity (Fig. 4d). The quantification of PET signals in all three mice showed increased tracer uptake in the ipsilateral axillary region of interest over the contralateral side (Fig. 4e). *Ex vivo Renilla* luciferase bioluminescence signals of the isolated lymph nodes again confirmed the presence of disseminated tumor cells in all three mice examined (Fig. 4f). Collectively, the data suggest that this tumor-directed vector delivery method seems to reach the SLN efficiently, reinforcing the potential use of adenovirus as a lymphangiographic mapping agent in ascertaining nodal status.

Detecting lymph node metastasis in an orthotopic xenograft

The intraprostatic implanted LAPC-9–VEGF-C–GFP–RL tumors show an extensive network of peritumoral lymphatics extending into the margin of the tumor (Fig. 5a). Notably, even

without forced VEGF-C expression, the orthotopic implanted LAPC-9 and CWR22Rv-1 prostate tumors showed extensive peritumoral lymphatics (Supplementary Fig. 2 online). However, the incidence of lymphatic metastasis in these models is less predictable than in the LAPC-9–VEGF-C model. Therefore, we used the VEGF-C overexpression model to facilitate detection of metastasis.

Fifteen days after tumor implantation, we injected mice with AdTSTA-fl in each footpad to target lymph nodes involved in prostate cancer metastasis (that is, inguinal, iliac and lumbar) [18]. Imaging of the whole mouse showed prominent *Renilla* luciferase signal emanating from the orthotopic tumor (Fig. 5b). Vector-directed firefly luciferase signals were able to identify the superficial nodes. However, owing to the photon scattering limitations, optical signals emanating from the deeper pelvic nodes would be difficult to discern in whole-animal imaging. Thus, we harvested the regional lymph nodes and imaged them *ex vivo*, and the periaortic node had the highest firefly luciferase signal (Fig. 5c). Histological examination of this node showed a focus of subcapsular metastasis (Fig. 5d), which was verified by human cytokeratin staining. To estimate the lesion size and the number of tumor cells in this involved node, we sectioned through the entire node. The maximum diameter of the lesion was ~250 μm, containing ~400 tumor cell nuclei in the largest section, which gives a conservative estimate of a maximum of 4,000 tumor cells in the entire lesion.

DISCUSSION

The status of lymph node metastasis is crucial for prostate cancer staging and treatment planning. However, the current procedures for acquiring this information are imprecise and invasive. A one-step, noninvasive imaging technology that can specifically visualize SLN metastasis would be of great value to the field. In this study, a recombinant replication-defective adenovirus served as the vehicle to deliver an imaging reporter gene to the tumor cells. An essential component of this technology is the ability of the adenovirus to function as a lymphotropic agent that is transported effectively to the draining lymph nodes as a free and infectious particle capable of transducing resident tumor cells and visualizing both large macroscopic and occult nodal lesions. We surmised that it is the robust, yet prostate-selective expression capability of the amplified TSTA vector that enables the direct imaging of the nodal metastases[16,17,21]. In one application, tumor-directed administration of the PET reporter vector (AdTSTA-sr39tk) produced specific ^{18}FHBG PET signals in the involved SLNs. To our knowledge, this is the first report detailing the lymphotropic and the selective gene expression capability of adenoviral particles to directly detect nodal metastases with PET. Although the issues regarding imaging sensitivity remain to be fully elucidated, the results presented here (Fig. 3c) suggest that this genetic biomarker–based PET was able to decisively seek out lymph node metastasis in a mouse bearing 2.5-mm lymph node lesions. Currently, the clinical lymphotropic MRI (LMRI) method is capable of detecting lesions 5–10 mm in diameter[8]. Furthermore, the results of tumor-directed AdTSTA-sr39tk administration (Fig. 4c) suggest that this technology has the potential to directly image microscopic metastases.

Extensive studies show that intravenous administration of adenoviral vectors results in substantial vector sequestration in the liver and reticuloendothelial system[13,24]. This biodistribution pattern points to the ineffectiveness of adenovirus to target lymphatic circulation after systemic administration. In contrast, historical evidence indicates an innate affinity of adenovirus for the lymphatic system. Adenovirus can produce persistent infections in lymphoid organs such as the adenoid, from which the first adenovirus was isolated[13]. An additional advantage of the adenoviral vector–mediated gene transfer approach is the prospect of inducing tumoricidal activity. For example, in addition to functioning as a PET reporter gene, the gene encoding the sr39tk reporter also acts as a suicide gene in the presence of the prodrug ganciclovir[25]. In fact, we have previously used the dual PET imaging and therapeutic

function of AdTSTA-sr39tk to treat prostate tumors[21]. It is also noteworthy that a wide range of tissue- and tumor-specific promoters have been successfully incorporated in adenoviral vectors to target selective types of cancer[14,26]. With this issue in mind, we recently developed a TSTA vector driven by the tumor-selective mucin-1 promoter and showed its feasibility in detecting SLN metastasis in an orthotopic breast tumor model (S. Huyn, J.B.B., M.S. and L.W., unpublished data). Hence, the adenoviral lymphangiographic imaging technology described in this study could be readily applied to melanoma and breast cancer, where determination of SLN status is also a key component of treatment planning.

Recent studies by our group and others have suggested that lymphatic dissemination also promotes subsequent systemic metastasis in experimental models[22,27–29]. Clinical experience suggests that meticulous pelvic lymph node resection not only provides diagnostic information but also has a positive impact on prolonging disease-free survival[30]. Collectively, these findings highlight the necessity for accurate noninvasive detection of lymph node metastasis. The current gene expression– and biomarker-based method holds promise to improve the specificity of diagnostic imaging of nodal metastasis of prostate cancer. Moreover, coupling detection and suicide-gene therapy would enable not only the accurate assessment of lymph node status, but also the prospect of preventing metastatic outgrowth and systemic spread. Therefore, we consider this study is of utmost clinical relevance and expect it to have considerable influence on the development of new diagnostic and therapeutic options for men with prostate cancer.

METHODS

Mouse handling

All handling of mice was performed in accordance with the University of California, Los Angeles Animal Research Committee guidelines.

Adenoviral constructs and lymphatic trafficking

The construction and propagation of adenoviral vectors has been described previously[17]. AdTSTA-fl was labeled with succinimidyl esters amine-reactive Alexa-Fluor 555 (AF555) fluorescent dye according to the manufacturer's recommendations (Molecular Probes/Invitrogen). Twenty-four hours after injecting AF555–AdTSTA-fl virus (1×10^7 PFU per 10 μl) in the forepaw, we harvested the mouse's axillary and brachial lymph nodes, mounted them as 4-μm frozen sections, briefly fixed them with ice-cold methanol and stained them with DAPI (Vector Laboratories). We verified the presence of viral particles with a Carl Zeiss LSM 310 laser scanning confocal microscope.

To isolate virus particles from lymph nodes, we injected mice ($n = 3$) in the forepaw with 1×10^8 PFU AdTSTA-fl (20 μl in PBS). We dissected lymph nodes and placed them in microcentrifuge tubes with 250 μl of RPMI medium. We disrupted nodal capsules by gentle agitation followed by brief vortexing and centrifugation at 2,500*g* for 5 min. We removed the supernatants and applied them to 1×10^5 LNCaP cells per well growing in a 24-well plate. We measured luciferase activity 4 d after infection by *in vitro* bioluminescence assay (Promega). We measured total protein by Coomassie Plus protein assay (Pierce Biotechnology).

Intraprostatic adenovirus administration

We exposed the prostates of 10-week-old $Pten^{-/-}$ mice by making a small abdominal incision and gently exposing the seminal vesicles. We injected the enlarged dorsolateral prostate with 1×10^8 PFU adenovirus per lobe, followed by closure of the surgical incision. After 1 h, we killed the mice and dissected regional periaortic, renal and mesenteric lymph nodes.

Real-time PCR

We harvested lymph nodes and extracted total DNA by a column purification procedure according to the manufacturer's suggested protocol (DNeasy Kit, Qiagen). We used purified adenovirus DNA (1×10^8 PFU) as a standard curve. We amplified exactly 2 μl per sample in triplicate with primers specific for the E2 region of adenovirus as previously described[13]. Reactions were run in an Opticon Monitor 2 real-time PCR machine (MJ Research, Bio-Rad) for 39 cycles of 95 °C for 15 s, 60 °C for 30s and 72 °C for 30 s.

Xenograft model of lymph node metastasis

We maintained the LAPC-9 xenograft by serial passage in SCID/Beige (natural killer cell–deficient) mice (Taconic). We processed freshly dissected LAPC-9 tumors (1,000 mm^3) into single-cell suspensions[17] and transduced them with the designated lentivirus, pCCL-VEGFC-IRES-GFP and pCCL-RL[22]. LAPC-9–VEGF-C cells (1×10^6) were implanted with Matrigel (BD Biosciences) on the right shoulder of SCID/Beige mice. We allowed the tumors to reach the ethical limit of 1.5 cm in diameter, at which point we performed tumor resection or killed the mice. We monitored metastasis after tumor resection for up to an additional 40 d by palpation, optical imaging of *Renilla* luciferase activity or ^{18}FLT PET imaging. For the orthotopic model, we injected 2.5×10^5 LAPC-9–VEGF-C–GFP–RL cells with Matrigel into each dorsolateral prostatic lobe.

Mouse imaging experiments

We injected mice in the paw with 20 μl of adenovirus in PBS and then gently massaged the paw for 5 min. We imaged mice 4 d after virus administration. Briefly, mice were anesthetized, injected with D-luciferin (150 mg kg^{-1} intraperitoneally) and imaged with a bioluminescent imager (IVIS 100; Xenogen) after 20 min. We analyzed data with IGOR-PRO Living Image software as described previously[20]. For PET studies, we injected mice ($n = 3$) with macroscopic lymph node metastases in the forepaw with AdTSTA-sr39tk (2×10^8 PFU). We injected mice receiving peritumoral administration of AdTSTA-sr39tk with 1×10^8 PFU (30 μl) every day for 5 d. Six days after the first or only injection of AdTSTA-sr39tk, we imaged the mice by PET after having given them a single intravenous bolus (~250 μCi) of ^{18}FHBG or ^{18}FLT. One hour after tracer injection, we scanned the mice for 10 min in a Focus 220 micro-PET scanner (Siemens Preclinical Solutions). PET images were created by filtered back projection at 0.4-mm pixel size with 0.8-mm slice thickness. We then transferred the mice to a micro-CT scanner (MicroCAT II, Siemens Preclinical Solutions) and imaged them over 7 min using 70-kVp, 500-ms exposures and 360° rotation to create images with 200-micron voxel size. We created fused PET-CT images with previously described methods[31].

Positron emission tomography and computed tomography analysis

We analyzed PET and CT datasets with AMIDE software[32]. All PET datasets were converted to percentage injected dose per gram on the basis of a phantom calibration constant, total injected dose, decay rate for ^{18}F and an assumption of 1 g ml^{-1} tissue density. We drew regions of interest over the site of injection as well as on ipsilateral and contralateral axilla. We used the average of the maximum pixel values from representative regions to calculate percentage injected dose per gram.

Immunohistochemistry

We fixed tissues in 3% paraformaldehyde and embedded them in paraffin. We stained sections (5 μm) with antibody to the epithelial marker cytokeratin (Biogenex) or to the lymphatic marker Lyve-1 (RELIATech) as previously described[22]. We detected horseradish peroxidase–conjugated secondary antibody to the cytokeratin antibody with 3,3-diamino-benzidine tetrahydrochloride substrate (Liquid DAB Substrate Pack, Biogenex). We performed

macrophage staining with rat antibody to mouse F4/80 (Serotec). We detected red fluorescent protein (RFP) from paraffin-embedded sections with rabbit antibody to RFP (Rockland Immuno-chemicals). We performed secondary detection of F4/80 and RFP with biotinylated antibodies to mouse and rabbit IgG, respectively (Vector Laboratories).

Rabbit antibody to herpes simplex virus thymidine kinase (HSV-tk) was a kind gift from M. Black, and we used it on 3% paraformaldehyde-fixed, paraffin-embedded tissue sections by incubating it at a 1:15,000 dilution overnight at 4°C. We used multilink antibody (1:20, Biogenex) for secondary detection.

Statistical analyses

All error bars in graphical data represent means ± s.e.m. We used Student's two-tailed *t*-test for determination of statistical relevance between groups and considered $P < 0.05$ significant.

Supplementary Material

Refer to Web version on PubMed Central for supplementary material.

Acknowledgments

We thank M.E. Black (Washington State University) for antibody to HSV-tk. We appreciate the discussions provided by E. Brakenhielm, A. Cochran and J. DeKernion. This work is supported by the US National Cancer Institute Specialized Programs of Research Excellence (SPORE) program grants P50 CA092131 and RO1 CA101904-01, US Department of Defense grant DAMD17-03-1-0095 and the Prostate Cancer Foundation (to L.W.) and by US National Cancer Institute grant 2U24 CA092865 (to A.F.C.). J.B.B. is supported by UCLA Research Training in Pharmacological Sciences grant T32-GM008652 and US Department of Defense grant CDMRP 07-1-0064. We are indebted to the technical support provided by W. Ladno, J. Edwards and A. Luu of Crump Institute of Molecular Imaging.

References

1. Roehl KA, Han M, Ramos CG, Antenor JA, Catalona WJ. Cancer progression and survival rates following anatomical radical retropubic prostatectomy in 3,478 consecutive patients: long-term results. J Urol 2004;172:910–914. [PubMed: 15310996]
2. Epstein JI, Partin AW, Potter SR, Walsh PC. Adenocarcinoma of the prostate invading the seminal vesicle: prognostic stratification based on pathologic parameters. Urology 2000;56:283–288. [PubMed: 10925095]
3. Daneshmand S, et al. Prognosis of patients with lymph node positive prostate cancer following radical prostatectomy: long-term results. J Urol 2004;172:2252–2255. [PubMed: 15538242]
4. Link RE, Morton RA. Indications for pelvic lymphadenectomy in prostate cancer. Urol Clin North Am 2001;28:491–498. [PubMed: 11590808]
5. Heidenreich A, Ohlmann CH, Polyakov S. Anatomical extent of pelvic lymphadenectomy in patients undergoing radical prostatectomy. Eur Urol 2007;52:29–37. [PubMed: 17448592]
6. Rorvik J, Haukaas S. Magnetic resonance imaging of the prostate. Curr Opin Urol 2001;11:181–188. [PubMed: 11224749]
7. Wolf JS Jr, et al. The use and accuracy of cross-sectional imaging and fine needle aspiration cytology for detection of pelvic lymph node metastases before radical prostatectomy. J Urol 1995;153:993–999. [PubMed: 7853590]
8. Harisinghani MG, et al. Noninvasive detection of clinically occult lymph-node metastases in prostate cancer. N Engl J Med 2003;348:2491–2499. [PubMed: 12815134]
9. Giuliano AE, Kirgan DM, Guenther JM, Morton DL. Lymphatic mapping and sentinel lymphadenectomy for breast cancer. Ann Surg 1994;220:391–398. discussion 398–401 . [PubMed: 8092905]
10. Morton DL, et al. Sentinel-node biopsy or nodal observation in melanoma. N Engl J Med 2006;355:1307–1317. [PubMed: 17005948]

11. Szuba A, Shin WS, Strauss HW, Rockson S. The third circulation: radionuclide lymphoscintigraphy in the evaluation of lymphedema. J Nucl Med 2003;44:43–57. [PubMed: 12515876]
12. Ikomi F, Hanna GK, Schmid-Schonbein GW. Size- and surface-dependent uptake of colloid particles into the lymphatic system. Lymphology 1999;32:90–102. [PubMed: 10494521]
13. Johnson M, Huyn S, Burton J, Sato M, Wu L. Differential biodistribution of adenoviral vector *in vivo* as monitored by bioluminescence imaging and quantitative polymerase chain reaction. Hum Gene Ther 2006;17:1262–1269. [PubMed: 17117891]
14. Kishimoto H, et al. *In vivo* imaging of lymph node metastasis with telomerase-specific replication-selective adenovirus. Nat Med 2006;12:1213–1219. [PubMed: 17013385]
15. Labow D, Lee S, Ginsberg RJ, Crystal RG, Korst RJ. Adenovirus vector–mediated gene transfer to regional lymph nodes. Hum Gene Ther 2000;11:759–769. [PubMed: 10757355]
16. Iyer M, et al. Two-step transcriptional amplification as a method for imaging reporter gene expression using weak promoters. Proc Natl Acad Sci USA 2001;98:14595–14600. [PubMed: 11734653]
17. Wu L, et al. Chimeric PSA enhancers exhibit augmented activity in prostate cancer gene therapy vectors. Gene Ther 2001;8:1416–1426. [PubMed: 11571582]
18. Tilney NL. The systemic distribution of soluble antigen injected into the footpad of the laboratory rat. Immunology 1970;19:181–184. [PubMed: 5484787]
19. Wang S, et al. Prostate-specific deletion of the murine *Pten* tumor suppressor gene leads to metastatic prostate cancer. Cancer Cell 2003;4:209–221. [PubMed: 14522255]
20. Adams JY, et al. Visualization of advanced human prostate cancer lesions in living mice by a targeted gene transfer vector and optical imaging. Nat Med 2002;8:891–897. [PubMed: 12134144]
21. Johnson M, et al. Micro–PET-CT monitoring of herpes thymidine kinase suicide gene therapy in a prostate cancer xenograft: the advantage of a cell-specific transcriptional targeting approach. Mol Imaging 2005;4:463–472. [PubMed: 16285908]
22. Brakenhielm E, et al. Modulating metastasis by a lymphangiogenic switch in prostate cancer. Int J Cancer 2007;121:2153–2161. [PubMed: 17583576]
23. Klein KA, et al. Progression of metastatic human prostate cancer to androgen independence in immunodeficient SCID mice. Nat Med 1997;3:402–408. [PubMed: 9095173]
24. Tao N, et al. Sequestration of adenoviral vector by Kupffer cells leads to a nonlinear dose response of transduction in liver. Mol Ther 2001;3:28–35. [PubMed: 11162308]
25. Rosenfeld ME, et al. Adenoviral-mediated delivery of the herpes simplex virus thymidine kinase gene selectively sensitizes human ovarian carcinoma cells to ganciclovir. Clin Cancer Res 1995;1:1571–1580. [PubMed: 9815958]
26. Sadeghi H, Hitt MM. Transcriptionally targeted adenovirus vectors. Curr Gene Ther 2005;5:411–427. [PubMed: 16101515]
27. Roberts N, et al. Inhibition of VEGFR-3 activation with the antagonistic antibody more potently suppresses lymph node and distant metastases than inactivation of VEGFR-2. Cancer Res 2006;66:2650–2657. [PubMed: 16510584]
28. Cao Y. Opinion: emerging mechanisms of tumour lymphangiogenesis and lymphatic metastasis. Nat Rev Cancer 2005;5:735–743. [PubMed: 16079909]
29. Lin J, et al. Inhibition of lymphogenous metastasis using adeno-associated virus–mediated gene transfer of a soluble VEGFR-3 decoy receptor. Cancer Res 2005;65:6901–6909. [PubMed: 16061674]
30. Bader P, Burkhard FC, Markwalder R, Studer UE. Disease progression and survival of patients with positive lymph nodes after radical prostatectomy. Is there a chance of cure? J Urol 2003;169:849–854. [PubMed: 12576797]
31. Chow PL, Stout DB, Komisopoulou E, Chatziioannou AF. A method of image registration for small animal, multimodality imaging. Phys Med Biol 2006;51:379–390. [PubMed: 16394345]
32. Loening AM, Gambhir SS. AMIDE: a free software tool for multimodality medical image analysis. Mol Imaging 2003;2:131–137. [PubMed: 14649056]

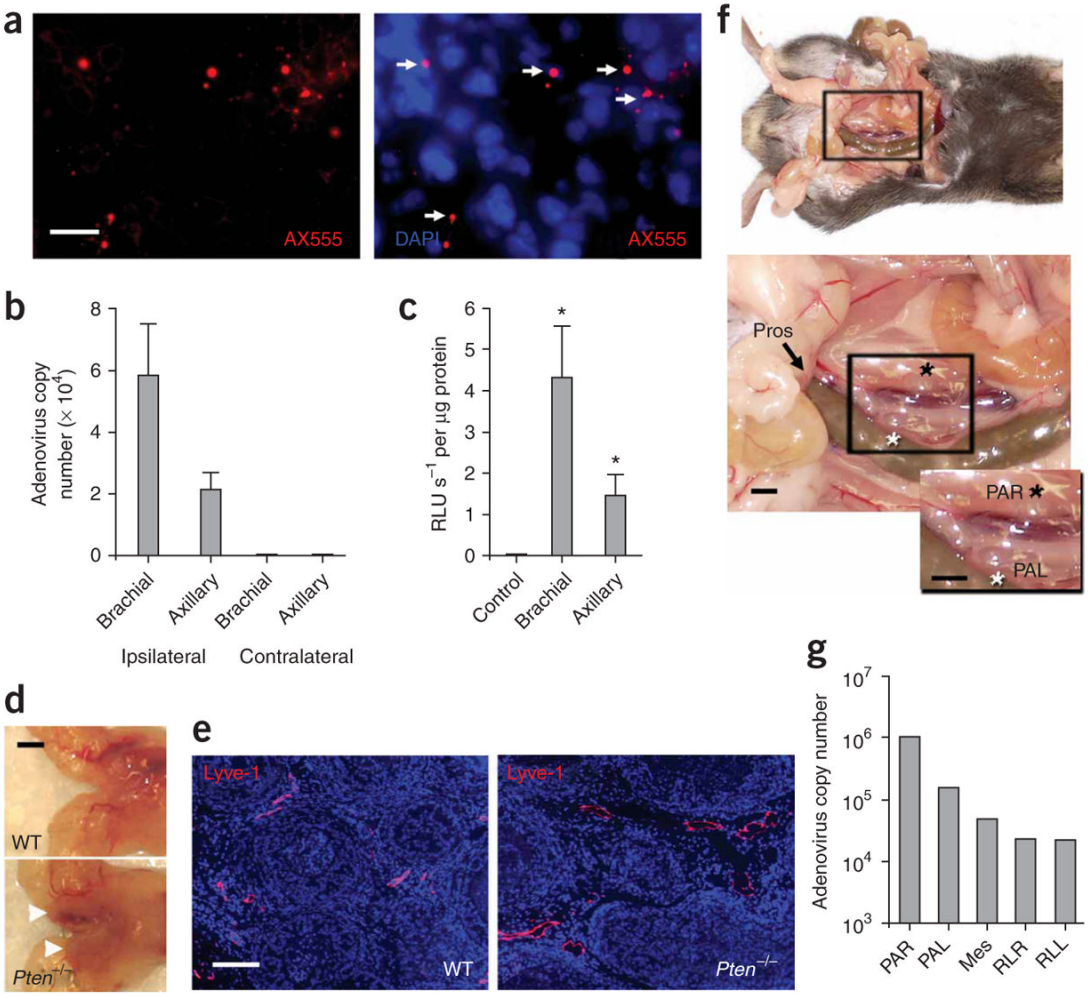

Figure 1.

Adenovirus as a lymphotropic particle. (**a**) Virus conjugates (red, white arrows) and lymphocyte nuclei (DAPI, blue) in thin sections of the brachial node after injection of fluorescent-labeled AF555–AdTSTA-fl (1×10^7 PFU, 10 µl) in the paw. (**b**) Real-time PCR analysis of DNA extracted from axillary and brachial lymph nodes 24 h after forepaw injection of 1×10^8 PFU of AdTSTA-fl vectors. No viral DNA was detected in contralateral lymph nodes within 39 PCR cycles. (**c**) Luciferase activity 4 d after *in vitro* infection of LNCaP cells with AdTSTA-fl recovered from lymph nodes. Luminescence per second (RLU s^{-1}) was normalized to total protein concentration. (**d**) Gross anatomical detail of a *Pten*$^{-/-}$ mouse's prostate lobes (white arrows) compared to a wild-type littermate. (**e**) Lyve-1 staining of lymphatic vessels in *Pten*$^{-/-}$ mice compared to wild-type mice. Pros., prostate. (**f**) Anatomy of the periprostatic region reveals the close proximity of the two periaortic lumbar nodes (white asterisk, left periaortic lumbar node (PAL); black asterisk, right periaortic lumbar node (PAR)). Each black box highlights the enlarged region in the inset. (**g**) Real-time PCR analysis of regional lymph nodes 1 h after injection of 1×10^8 PFU of AdTSTA-fl into each prostatic lobe (Mes, mesenteric; RLR, renal node right; RLL, renal node left). Error bars (**b**,**c**) are means ± s.e.m., $n = 4$ mice; in **c**, brachial $^*P = 0.014$ and axillary $^*P = 0.032$, compared to control. Scale bars, 10 µm (**a**); 2 mm (**d**,**f**); 200 µm (**e**).

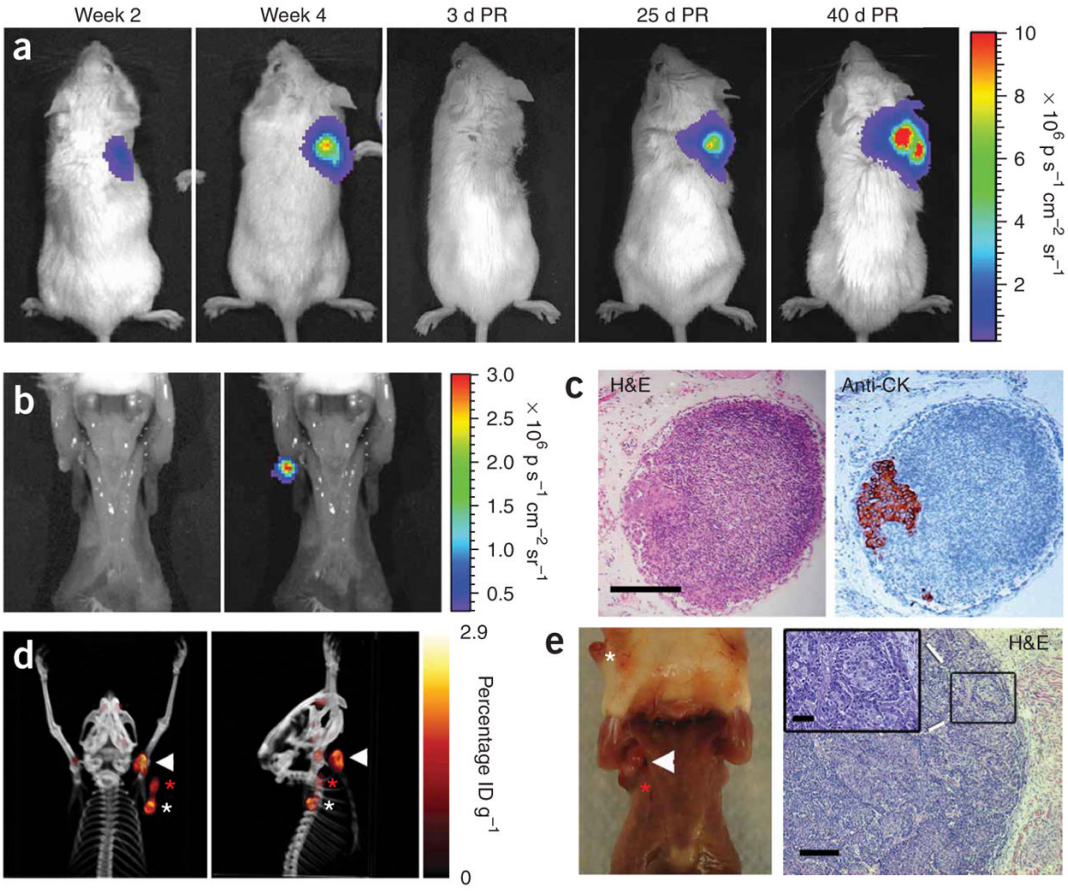

Figure 2.

Monitoring lymph node metastasis in a prostate cancer xenograft model. (**a**) Representative images of a mouse with LAPC-9–VEGF-C–GFP–RL tumor cells grafted on the right shoulder to promote metastasis to brachial and axillary lymph nodes. The kinetics of tumor growth can be monitored by bioluminescence imaging of *Renilla* luciferase–expressing tumor cells. Color bar represents photons s^{-1} cm^{-2} steradian^{-1} (p $s^{-1}cm^{-2}$ sr^{-1}); PR, post-resection.

(**b**) Bioluminescence (*Renilla* luciferase activity) in the exposed ipsilateral axillary lymph node of a mouse with a tumor 4 weeks after implantation. Left, photo; right, overlay. (**c**) Histological analysis of the photon-emitting lymph node in **b** shows a subcapsular microscopic lesion as visualized by staining with H&E (left) and with an antibody to human cytokeratin (anti-CK; right).

(**d**) PET-CT imaging with ^{18}FLT at 30 d after resection of the primary tumor shows extensive metastasis (color bar represents percentage injected dose per gram, ID g^{-1}). (**e**) Photograph (left) of this mouse shows extensive metastasis in the ipsilateral primary axillary (white arrowhead) and accessory axillary (red asterisk) lymph nodes. The primary tumor regrowth (white asterisk) is also present. H&E staining (right) shows extensive infiltration by tumor cells, distending the axillary lymph node. Higher magnification inset (inset) of boxed region shows that tumor cells make up most of the population. Scale bars, 200 μm (**c**,**e** right), 50 μm (**e**, right inset).

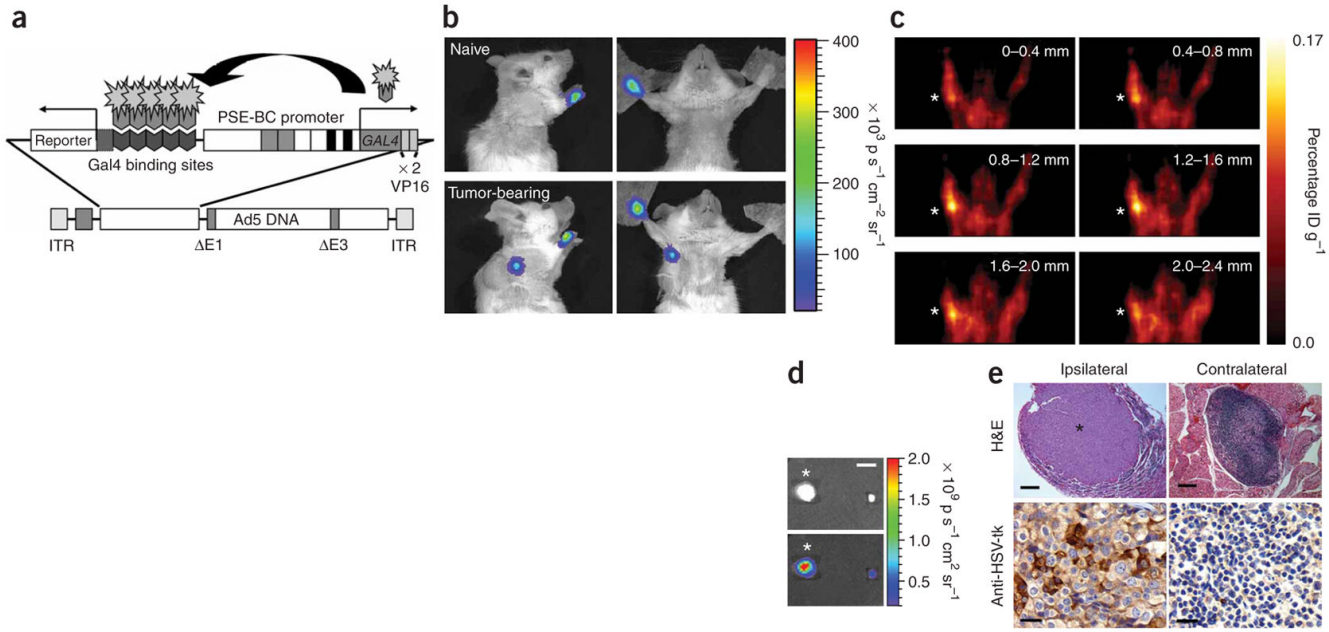

Figure 3.

TSTA adenovirus–mediated detection of macroscopic lesions in lymph nodes by optical and PET imaging. (**a**) A schematic representation of the TSTA adenoviral vectors used to detect nodal metastases. PSE-BC is an enhanced PSA-based promoter containing additional AR enhancer elements as previously described[17]. The binary prostate-specific TSTA expression cassette is inserted into the E1 region of the viral genome. The firefly luciferase or enhanced variant of the herpes simplex virus thymidine kinase (*sr39tk*) are used as reporter genes. (**b**) Firefly luciferase signal is seen in the axillary region of tumor-bearing mice, but not in naive animals, at 4 d after injection with AdTSTA-fl (1×10^7 PFU). p, photons. (**c**) AdTSTAsr39tk (1×10^8 PFU per paw) was injected in each forepaw of mice at 30 d after tumor resection. Sequential coronal sections through the axillary region of a mouse show specific PET signal detected ipsilaterally (asterisk). ID, injected dose. (**d**) Fluorescent overlay in dissected brachial lymph nodes show the presence of GFP-expressing tumor cells in the ipsilateral (left) but not the contralateral (right) lymph node. (**e**) H&E-stained section of a large tumor mass (asterisk) within the ipsilateral brachial node (top left). No metastasis could be detected in the contralateral lymph node (top right). HSV-tk–positive tumor cells (brown) were observed in the ipsilateral lymph node (bottom left), but not in the contralateral nodes (bottom right). Scale bars, 2 mm (**d**); 200 μm (**e**, top panels); 20 μm (**e**, bottom panels).

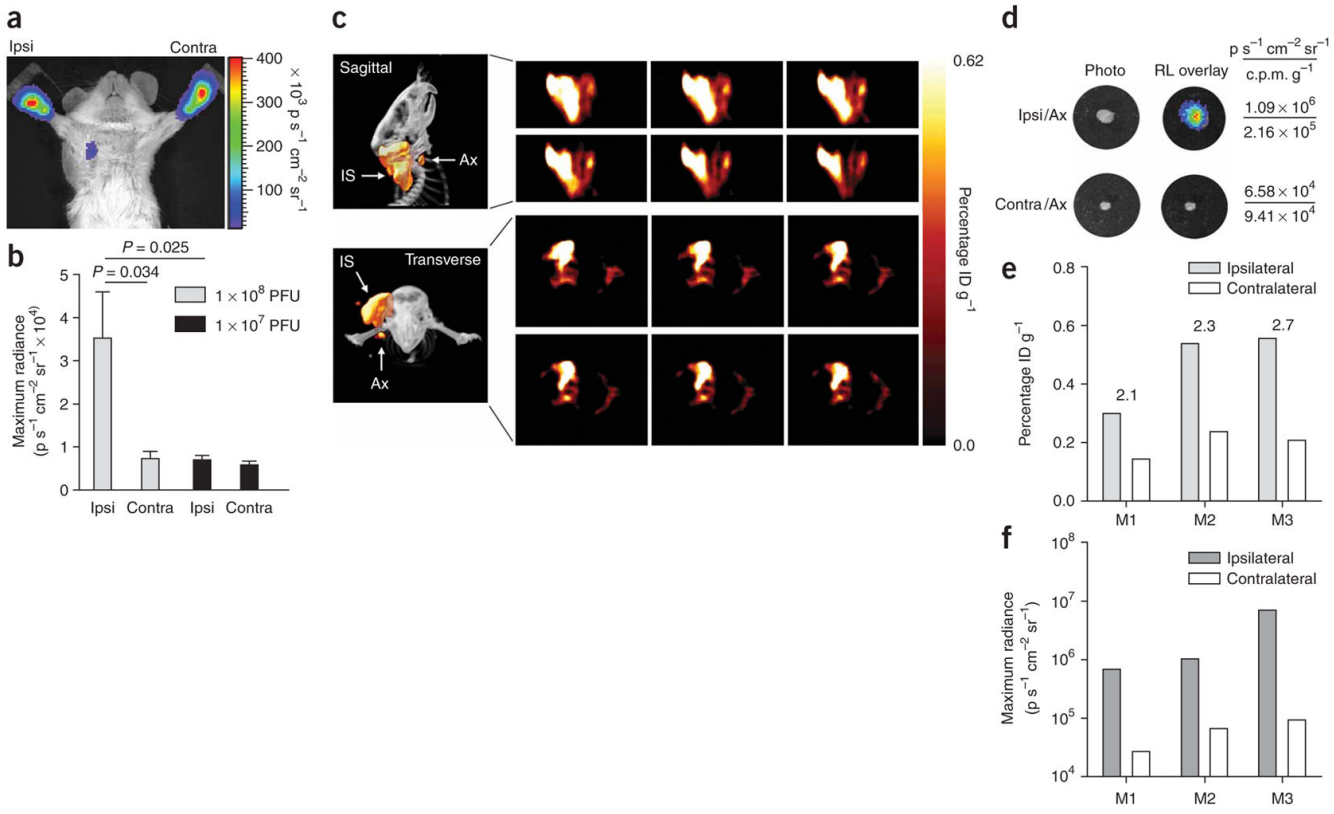

Figure 4.

Detection of occult lymph node metastasis with bioluminescence and PET imaging. (**a**) A tumor-bearing mouse showing firefly luciferase activity in the ipsilateral (ipsi), but not contralateral (contra) axilla 3 d after injection of 1×10^8 PFU AdTSTA-fl into each forepaw. (**b**) Quantification of optical signal intensity in mice bearing LAPC9–VEGF-C–GFP tumors at ~1.0 cm diameter and injected with either 1×10^7 ($n = 6$) or 1×10^8 ($n = 6$) PFU of AdTSTA-fl in both forepaws. (**c**) Representative sagittal (top left) and transverse (bottom left) PET-CT images show PET signal emitted from the tumor injection site (IS) and the draining axillary sentinel lymph node (Ax) after tumor-directed injection of AdTSTAsr39tk (5×10^8 PFU in total). Consecutive 0.4-mm tomographic frames (right) through the region of interest in the right axilla: sagittal frames, top two rows; transverse frames, bottom two rows. (**d**) *Ex vivo* optical and radioactive signal in ipsilateral (ipsi/ax) and contralateral (contra/ax) axillary nodes from the mouse depicted in **c** correlating the optical signal with the ^{18}FHBG uptake. CPM g^{-1}, counts per minute per gram tissue. (**e**) Comparative ^{18}FHBG uptake values for ipsilateral and contralateral axilla in all three mice (M1, M2 and M3) examined. Above each pair of bars is the ratio of ipsilateral to contralateral lymph node values. ID, injected dose. (**f**) *Ex vivo* optical signal (*Renilla* luciferase) for each axillary lymph node from the same mice as in **e**. Error bars (**b**) are means ± s.e.m.

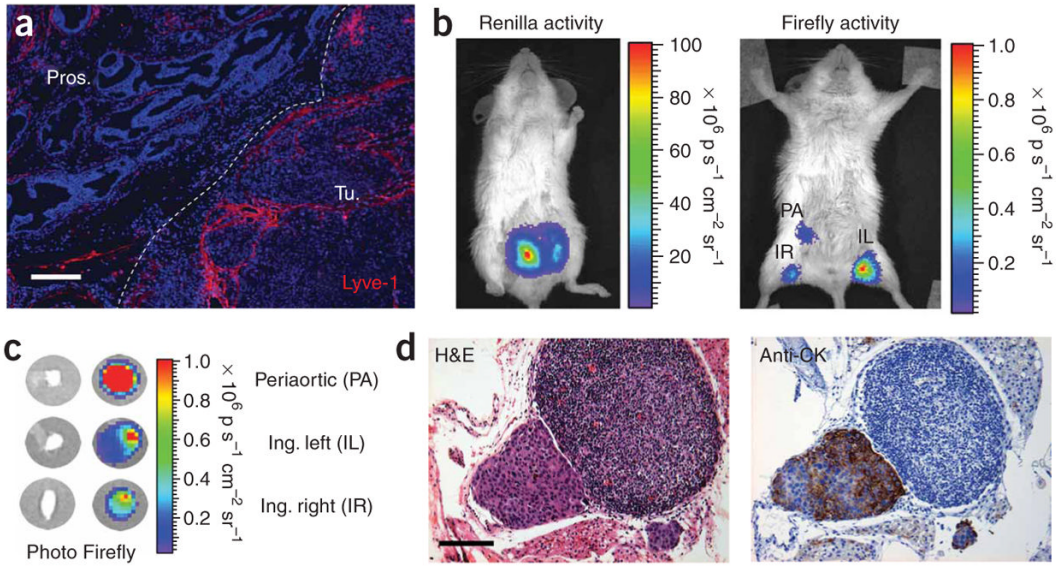

Figure 5.

Detection of occult LN metastasis in orthotopic xenograft model. (**a**) Immunohistochemistry of LAPC-9–VEGF-C–RL orthotopic tumor shows extensive lymphatic networks (red) along the margin (dotted white line) of the tumor (Tu.) extending intratumorally from the normal prostatic region (Pros.). (**b**) Representative optical image of *Renilla* luciferase expression (left) at 3 weeks after orthotopic implantation of 2.5×10^5 LAPC-9–VEGF-C–GFP–RL tumor cells per lobe in the prostate of SCID/Beige mice. Injection of 1×10^8 PFU AdTSTA-fl in both hind paws of mice carrying LAPC-9–VEGF-C–RL orthotopic tumors led to observable firefly luciferase signal (right) in inguinal (left, IL; right, IR) and periaortic (PA) regions at 4 d after viral injection. p, photons. (**c**) *Ex vivo* firefly luciferase bioluminescence activity of dissected nodes showed the highest optical signal in the isolated periaortic lymph node. Ing., inguinal. (**d**) Histological analysis (H&E) showed the presence of a subcapsular lesion within the periaortic lymph node. This mass was verified to be LAPC9 by staining with antibody to human cytokeratin (anti-CK) in a consecutive section. Scale bars, 200 μm (**a**); 100 μm (**d**).